Time-resolved x-ray studies of the dynamics of smectic-*A* layer realignment by magnetic fields

P. D. Brimicombe,[1] S. D. Siemianowski,[1] S. Jaradat,[1] Y. K. Levine,[2] P. Thompson,[3] W. Bras,[4] and H. F. Gleeson[1,*]

[1]*School of Physics and Astronomy, University of Manchester, Manchester, M13 9PL, United Kingdom*

[2]*Debye Institut, Ornstein Laboratory, Utrecht University, 3508 TA Utrecht, The Netherlands*

[3]*XMaS, UK-CRG, European Synchrotron Radiation Facility, BP220, F-38043 Grenoble Cedex, France*

[4]*Netherlands Organisation for Scientific Research (NWO), Dubble GRG,European Synchrotron Radiation Facility, , BP220, 6 rue Jules Horowitz, F-38043 Grenoble, Cedex, France*

(Received 1 December 2008; revised manuscript received 9 February 2009; published 31 March 2009)

While the rotation of smectic layers under an applied field may at first appear to be a relatively simple problem, the dynamic processes involved are rather complex. An applied field produces a torque on the liquid crystal director, but has no direct influence on the smectic layers. If the director is reoriented significantly, however, the layers must also reorient in order to accommodate this (the layered structure is produced by short-range molecular interactions). Indeed, if the liquid crystalline order is not maintained during the realignment then matters become even more complex. In this paper we use time-resolved x-ray scattering to investigate the realignment of smectic-*A* layers in thin-film devices using a magnetic field. No evidence is found for continuous rotation of the smectic layers under any circumstances in such devices, a result that is not found when using bulk samples. No evidence indicating the formation of the nematic phase is observed during realignment. A molecular-dynamics technique is used to model the system which indicates that the sample becomes significantly disorganized during the realignment process when large angular rotations are induced.

DOI: 10.1103/PhysRevE.79.031706 PACS number(s): 42.70.Df, 61.30.Eb, 83.80.Xz, 61.05.cc

I. INTRODUCTION

The use of thermotropic liquid crystal materials in optoelectronic devices is widespread but it is only recently that devices that utilize smectic phases have been commercialized. Phases of this kind consist of a layered structure, with orientational order of the molecular long axes within the layers. While there have been many studies of smectic layer reorientation due to applied electric fields, these have mainly been restricted to the chiral smectic-*C* (Sm-C^*) phase [1–4] in which the average molecular axis (the director) is tilted with respect to the layer normal and there is a long-range helicoidal structure parallel to the layer normal. There have been further studies of this effect in the chiral smectic-*A* (Sm-A^*) phase in which the layer normal and the director are parallel, primarily close to the transition from Sm-A^* to Sm-C^* or a Sm-C^* subphase [5,6], and in the antiferroelectric and intermediate smectic phases [7]. In all of these cases, the rotation of the smectic layers is either parallel to the applied field or has been studied in the context of the chevron-to-bookshelf transition that occurs in thin-film ferroelectric liquid crystal devices. In each of these cases the rotation process is somewhat complex and involves a number of different contributing factors. When a field is applied to an achiral smectic liquid crystal phase there is no direct interaction between the layers and the field—a torque is produced on the liquid crystal director. If the director is reoriented sufficiently, the layers will have to reorganize in order to satisfy the short-range interactions that cause their formation. In order to investigate the relative influence of the longer-range interactions between the director and the applied field and the short-range interactions that induce layer formation, we will examine smectic-*A* (Sm-*A*) phase layer reorientation using magnetic fields. This system is conceptually simpler than those discussed above; the field is applied in the same plane as the rotation and the phase in question is achiral and of higher symmetry than the smectic-*C* phases. In addition we will examine this process in thin-film devices in order to investigate the influence of the confining surfaces.

NMR studies of magnetic field-induced layer realignment in the Sm-*A* phase of a deuterated version of material 8CB have indicated that the realignment process is highly dependent on the initial angle between the smectic layer normal and the applied magnetic field [8,9]. When the realignment is over an angle of less than ~45° the sample appears to rotate as a monodomain, with the smectic layers retaining their integrity during realignment. At angles above this threshold, however, the dynamics become significantly more complicated, with some evidence suggesting the formation of a multidomain structure. NMR, however, cannot be used to observe the orientation and integrity of the smectic layers directly since it only provides information about the orientation of the director.

Time-resolved x-ray scattering is a technique that has been widely used to observe the reorientation of smectic layers over time. Using this technique it has been shown that the reorientation process that occurs is strongly dependent on the temperature of the sample, with a distinctly faster response close to the Sm-*A* to nematic transition temperature of material 8CB [10]. In addition, when the rotation angle is larger than ~45°, two distinct realignment pathways were observed within a multidomain structure. Evidence for the presence of a multidomain structure during the reorganization of Sm-*A* layers under an applied electric field has also been reported in a slightly different geometry where the layers are rotated out of plane using an electric field [11,12].

In this paper we present the results of a time-resolved x-ray scattering experiment investigating the realignment of

*helen.gleeson@manchester.ac.uk

the Sm-*A* layers of liquid crystal mixture S3 induced by an applied magnetic field. In previous studies of this magnetic field induced reorganization very thick samples have been used in order to observe only bulk layer realignment. This may be problematic, however, since the length scales associated with liquid crystal alignment (a few hundreds of microns) are typically much smaller than the sample sizes used (some millimeters). During the experiment the director is initially aligned parallel to the applied field, producing a well-aligned monodomain due to the presence of the field. If the field is removed or is no longer aligned with the director, the sample is unlikely to remain in a monodomain because its thickness is far greater than the length scale of the liquid crystal alignment. In this study we have avoided this problem by investigating this realignment process in thin-film devices and investigating the influence of the surfaces on the realignment. Confinement of the sample in thin films may appear to be a small alteration to the experiment described in Ref. [10]. But it produces significant quantitative and qualitative differences in the realignment process as will become clear. In addition, the liquid crystal material is confined to thin films in conventional liquid crystal devices and it is therefore important to understand the influence of confining surfaces on the reorientation of smectic layers. A molecular-dynamics simulation technique is used to model the system and the results are compared to the experimental findings. Furthermore, we briefly investigate the influence of the surface treatment on the realignment phenomenon. These results shed new light on this complex realignment process and the influence of surface alignment and confinement on smectic layers.

II. EXPERIMENTAL METHOD

Time-resolved small-angle x-ray diffraction experiments were carried out at the DUBBLE beamline, BM26B at the European Synchrotron Radiation Facility (ESRF), Grenoble, France. Since the details of the beamline have been reported extensively elsewhere [13], only a brief description will be given here. The energy of the incident beam was tuned to 12.6 keV and the beamline optics provide a spot size of around 300×300 μm^2 and a maximum flux of approximately 1×10^{11} photons/s at this energy. A schematic diagram of the experimental setup is shown in Fig. 1. Thin film devices constructed using a pair of 100 μm thickness glass coverslips, separated by 170 μm thickness nylon spacers, and capillary-filled with the liquid crystal mixture S3 (Merck GmbH) are placed in a 2 T magnetic field (American Magnetics Inc.). It should be noted that the confinement of the sample between 100 μm thickness glass windows significantly reduces the x-ray flux incident on the liquid crystal sample (and also the scattered x-ray intensity). Even so, care must be taken to avoid degradation of the liquid crystal by the high energy x rays. In order to prevent damage to the sample the x-ray beam was only allowed to impinge onto the sample while measurements were being taken and the transition temperatures were monitored repeatedly during the experiment to ensure that no damage had occurred. Two types of devices are used: one set has clean untreated inner surfaces and the second has a thin layer of baked and unidirectionally rubbed polyvinyl alcohol (PVA) applied to each inner surface (during construction the rubbing directions of each substrate are aligned antiparallel). The device is positioned with the substrates approximately perpendicular to the incoming x-ray beam as shown in Fig. 1 so that the liquid crystal is confined to a thin ~170 μm thickness film perpendicular to the incident x rays. In previous experiments the samples used have been considerably larger (some millimeters in thickness) in order to observe only bulk effects [8–10]. The devices are attached to a custom-built brass hot stage that can be rotated in the plane perpendicular to the incoming x-ray beam using a belt-drive system attached to a stepper motor mounted outside the stray field produced by the magnet. The sample is heated in the presence of the magnetic field to either the nematic or isotropic phase and then cooled slowly into the Sm-*A* phase, producing high-quality uniform alignment of both the director and the layer normal parallel to the applied field (the diamagnetic anisotropy of this material is positive). The electron-density modulation due to the layering of the molecules then produces Bragg reflections since the angle of incidence is close to the Bragg angle (~0.9°) and the Bragg peaks in systems of this kind are typically quite broad [full width at half maximum (FWHM) of ~2°]. This leads to two first-order diffraction spots appearing on the area detector at the (0,0,1) and $(0,0,\bar{1})$ positions. The sample is then rotated rapidly in the same plane as the applied field by a fixed angle (ϕ), and the temporal evolution of the diffraction pattern is recorded during the layer realignment process with a resolution of 500 ms.

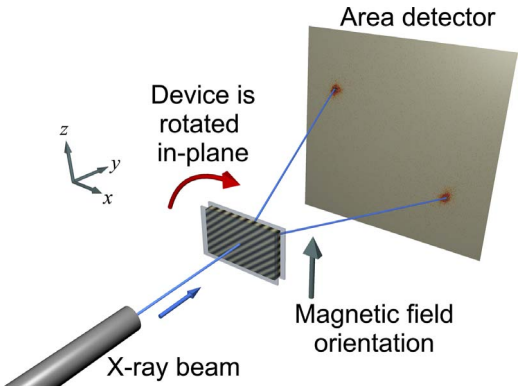

FIG. 1. (Color online) A schematic diagram of the experimental setup. The smectic layers scatter the incident x rays leading to two diffraction spots on the area detector on a line parallel to the layer normal. The device is rotated rapidly in the plane perpendicular to the incoming x-ray beam in the presence of an applied magnetic field and the time evolution of the diffraction pattern is recorded.

It would be advantageous to take a series of diffraction patterns for different angles of incidence between the incoming x-ray beam and the plane of rotation (rocking) since this would provide more information about the smectic layer distribution and orientation. This is not possible in this case, however, partly because of the geometrical restrictions of the magnet used, but also by the nature of the realignment process itself. The realignment dynamics can be substantially

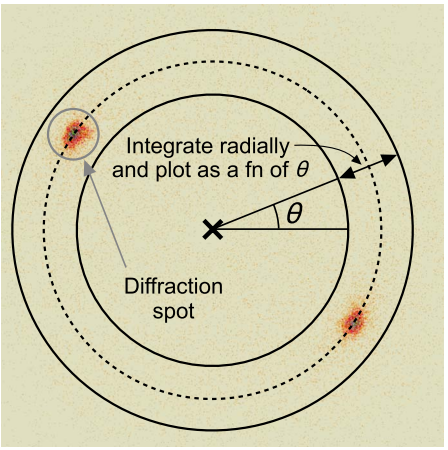

(a) Integration technique

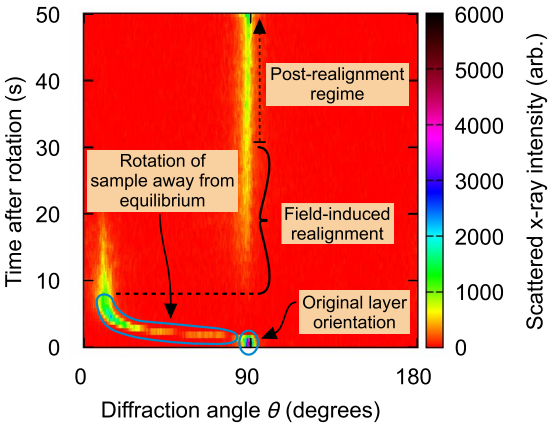

(b) Diffraction angle vs time

FIG. 2. (Color online) (a) Integration technique used to generate the diffraction angle vs time plots. (b) An example diffraction angle vs time plot showing the sample rotation and the subsequent reorientation process back to the original layer orientation.

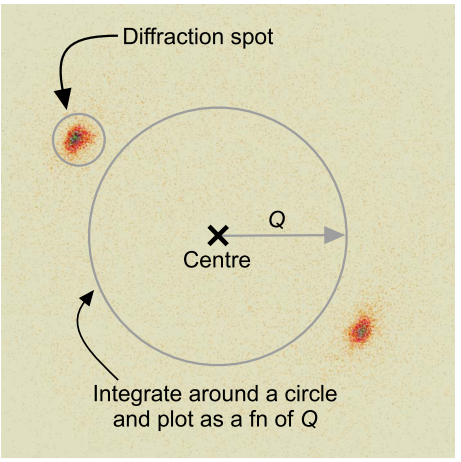

(a) Integration technique

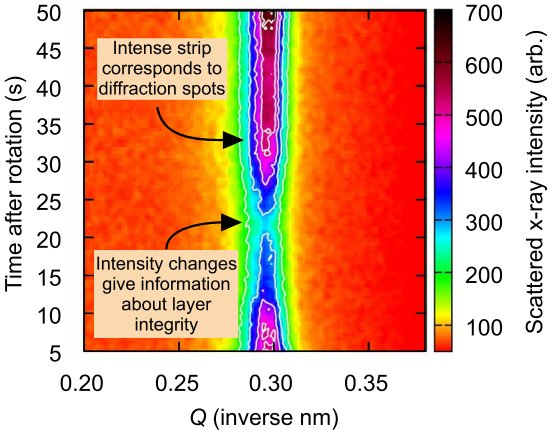

(b) Total intensity vs time

FIG. 3. (Color online) (a) Integration technique used to generate the total intensity vs time plots. (b) An example total intensity vs time plot. The center of the intense stripe corresponds to the Q associated with the layer spacing of the liquid crystal.

different from one data set to the next (see, for example, Ref. [10]) and so recombination of the data sets taken at a variety of different angles of incidence would be problematic.

III. DATA ANALYSIS TECHNIQUE

The analysis technique used here is similar to that used in Ref. [10]. Two different integration schemes are used in order to monitor the smectic layer orientation and the integrity of the layered structure. The first scheme is shown in Fig. 2(a). The diffraction pattern from the area detector is integrated radially over an annular strip surrounding the diffraction peaks, with the integrated intensity then plotted as a function of the azimuthal angle on the area detector [Fig. 2(b)]. This corresponds to the following integral:

$$f(\theta,t) = \int_{Q_1}^{Q_2} \Gamma(\theta,Q,t)dQ, \qquad (1)$$

where θ is the azimuthal angle on the area detector; Q is the distance from the center of the diffraction pattern; Q_1 and Q_2 are the inner and outer limits of the integration; t is time; and $\Gamma(\theta,Q,t)$ is the scattering intensity data. Initially the layer normal is parallel to the magnetic field, which is vertical, leading to diffraction spots at the θ=90° and 270° positions (the poles on the area detector pattern). The sample is then rotated in the plane perpendicular to the x-ray beam by an angle ϕ, and the angular orientation of the diffraction spots is tracked during this rotation and the subsequent layer realignment processes. An example of the output of such an integration is shown in Fig. 2(b) for a rotation angle of ϕ=78°, clearly indicating how the layer orientation changes as a function of time. Since the diffraction pattern is symmetric we only plot the first 180° (the peak intensities of the diffraction spots are typically different since, as discussed in Ref. [10], the sample will not be precisely perpendicular to the incident x-ray beam; we plot the more intense of the two spots).

The second integration scheme is shown in Fig. 3(a). The scattered intensity is integrated circularly and then plotted as a function of Q (the distance from the center of the diffraction pattern). Expressed mathematically,

$$g(Q,t) = \int_0^{2\pi} \Gamma(\theta,Q,t)d\theta. \quad (2)$$

Calibration of the Q axis was carried out using the well-known diffraction from a powder sample of silver behenate. Comparison of the total diffracted intensity before and after rotation is problematic since any small change in the angle of incidence of the x-ray beam will cause large changes in the intensity (as the angle of incidence approaches the Bragg angle, the intensity increases greatly), and precise alignment of the rotation axis with the incoming beam is virtually impossible. Once the sample rotation has been completed, however, the total diffracted intensity can be monitored during the field-induced realignment, providing information about the out-of-plane orientation, spacing, and integrity of the layers. Furthermore, the linewidth of the peaks is characteristic of the liquid crystal phase; in the nematic phase, for example, it is much wider because of the lack of long-range translational order.

IV. EXPERIMENTAL RESULTS

Unlike in previous studies where layer reorientation is observed over a relatively wide temperature range below the Sm-*A* to nematic phase-transition temperature (e.g., 10 °C in Ref. [14]), realignment only occurs within 2 °C of the Sm-*A* to nematic transition temperature in our experiment, regardless of the surface treatment used. Since the realignment only occurs in such a narrow temperature range, investigation of the temperature dependence of this process was not possible. In addition, the realignment processes involved appear to be significantly different from those previously studied using time-resolved x-ray scattering [10,15]. As described by previous authors, the realignment process is found to be highly dependent on the initial rotation angle ϕ.

When small rotation angles are used, there is typically no reorganization of the smectic layers, as shown in Fig. 4(a) where the initial rotation angle $\phi \approx 25°$. When there is no layer reorientation, there is typically no change in the total scattered intensity, as can be seen in Fig. 4(a)(ii).

A typical example of the reorientation process when $\phi \approx 90°$ is shown in Fig. 4(b). It is clear from Fig. 4(b)(i) that no continuous rotation of the smectic layers is observed—the intensity at the original position decreases and that at the new field-aligned position increases after an induction period of a few seconds. At no point is scattering observed from an intermediate in-plane layer orientation. This result can be interpreted in one of four ways: the layered structure of the phase is lost during reorientation; the layers are no longer oriented close to the Bragg condition, i.e., they rotate out of plane and then back in plane at the field-aligned position; a very large spread of different layer orientations is present in the sample, producing powder-pattern diffraction; or that the rotation of the layers occurs over a timescale much shorter than the data-acquisition rate (two frames per second). The latter case is unlikely, however, since experiments carried out into layer realignment using crossed magnetic and electric fields indicate a time scale of some hundreds of seconds [16], while those investigating rotation of the smectic layers out of the plane of the device using electric fields indicate a time scale of several seconds, even when high fields are used [11].

The length of the induction period that precedes the realignment process is somewhat unpredictable, varying from around 1–40 s. As described in Ref. [14] this is due to variations in the initial defect density in the sample. In that case it was suggested that during realignment the monodomain sample splits into a large number of smaller domains, a process that is seeded by the presence of defects in the initial alignment; if there was a large number of defects in the sample before realignment the induction period was seen to greatly reduce.

The realignment process is also accompanied by a sharp reduction in the total scattered intensity, followed by an increase to approximately its initial value once the process is completed, as can be seen in Fig. 4(b)(ii). Although the peak height decreases, the linewidth remains approximately constant throughout the experiment. While formation of the nematic or isotropic phases during realignment cannot be discounted, there is no evidence from the total scattered intensity that directly supports these hypotheses.

If the sample is rotated by an intermediate angle (i.e., $\phi \sim 45°$) the realignment process is often incomplete, as shown in Fig. 4(c). Some material remains at its initial orientation, even some minutes after the sample has been rotated. Once again, however, no in-plane rotation of the smectic layers is observed. A slight decrease in the total scattered intensity can be seen in Fig. 4(c)(ii) during the realignment process. The effect is less pronounced than before, however, since only part of the sample undergoes reorientation.

In the samples where the surfaces have been treated with polyvinyl alcohol alignment layers the entire process is less predictable. The final state after layer reorganization is typically less well ordered [see Fig. 5(a) in which there is a larger range of layer orientations present close to the final field-aligned position]. This is probably due to the additional competing influence of the alignment layer. Interestingly, no significant difference was observed in the length of the induction period between samples with no alignment layer and those with alignment layers. A shorter induction period might be expected in the latter since the orientation of the magnetic field and the easy axis of the alignment layer were different, possibly leading to more defects because of the competition between the two. This, however, was not the case, regardless of the rotation angle used. Preliminary experiments testing the influence of the relative orientations of the rubbing direction and the magnetic field indicate that the initial orientation of the sample has little effect on the outcome. As described above, however, the realignment process is unpredictable in samples with alignment layers, and further work is required to understand this process fully.

V. COMPUTATIONAL SCHEME

A numerical simulation method of the field-induced realignment of a smectic nanodroplet in an external magnetic field is described in detail in Ref. [17]. The method is based on the dissipative particle dynamics (DPD) framework, but requires relatively small alteration in order to mimic the ex-

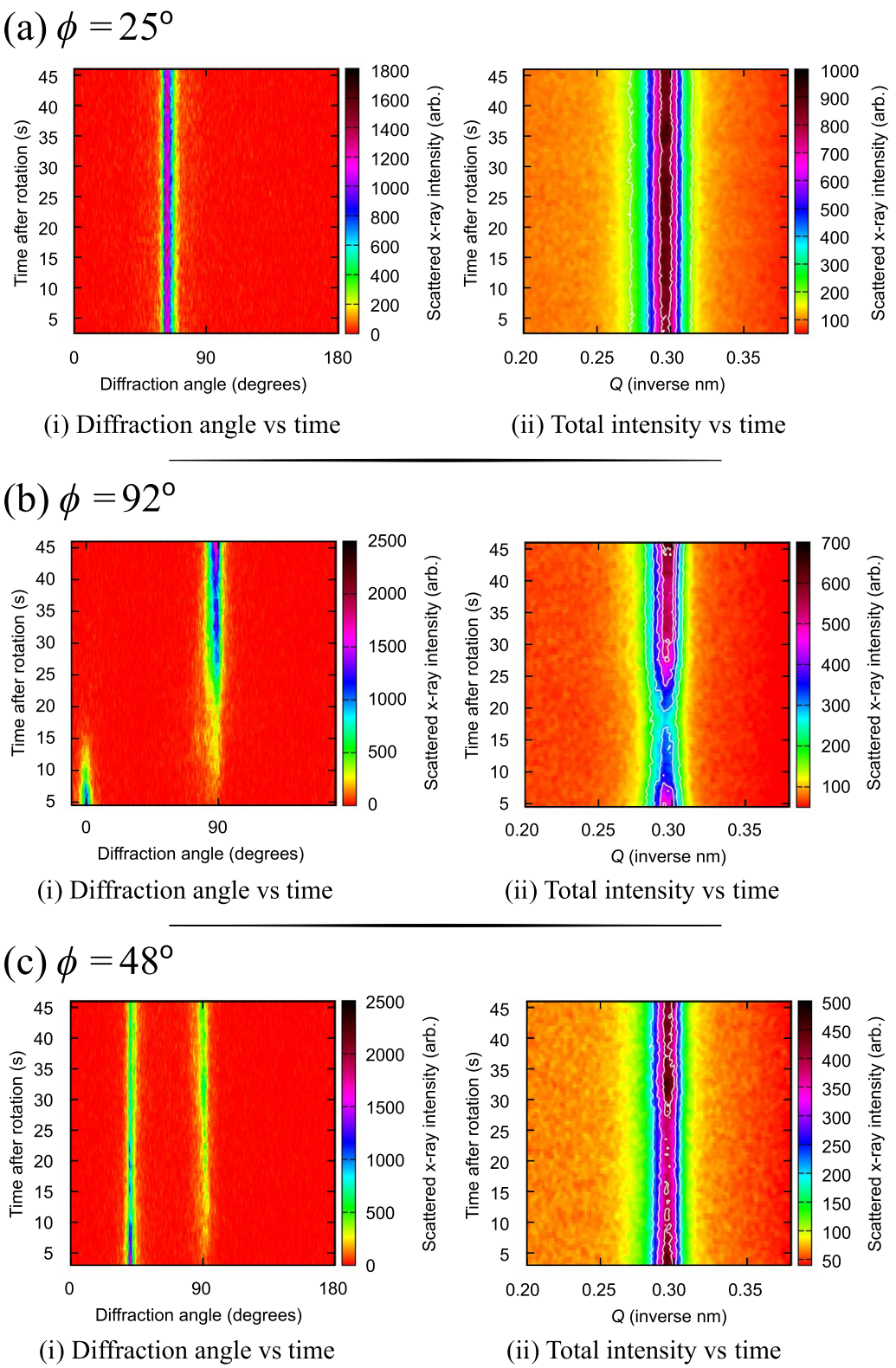

FIG. 4. (Color online) Typical layer realignment dynamics for various different rotation angles (a) $\phi \sim 25°$, (b) $\phi \sim 92°$, and (c) $\phi \sim 48°$. All of the devices tested have thicknesses of 170 μm and have no alignment layer applied to the glass surfaces. (a) Over small angular rotations, no layer realignment is observed. Previous authors have reported continuous rotation of the smectic layers under these conditions [8–10,14,15]. (b) When ϕ is close to 90° no rotation of the smectic layers is observed. During realignment, however, the total scattered intensity decreases significantly. (c) When using intermediate rotation angles the layer realignment is only partially completed. In all cases, the total intensity integral includes the signals from both diffraction peaks, reducing the sensitivity to rotations away from the Bragg condition.

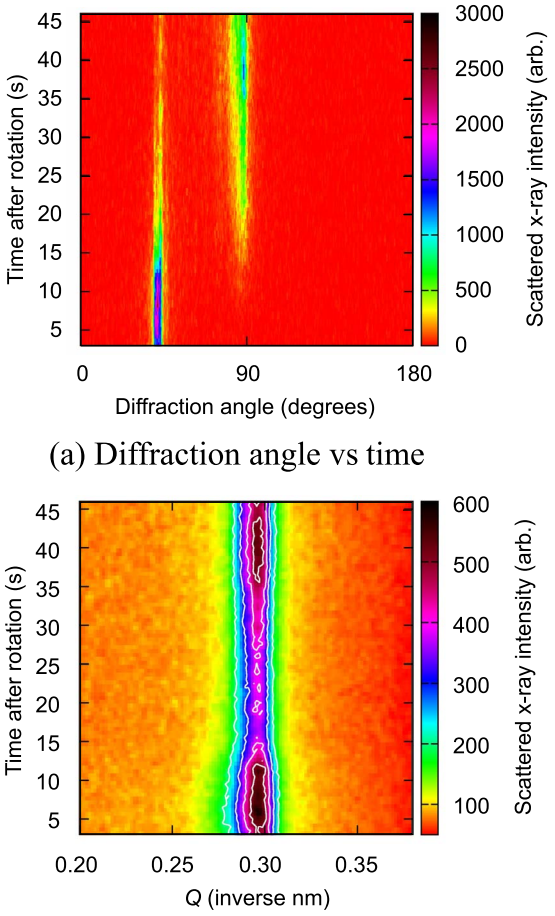

FIG. 5. (Color online) Typical results for an intermediate angular rotation $\phi \sim 49°$ in a 170 μm thickness device with rubbed polyvinyl alcohol alignment layers. The final state after realignment is typically less well ordered and the realignment is often more unpredictable.

perimental conditions used in this work. In particular, the sample now has a cylindrical shape, with its radius being larger than its thickness, the distance between its flat faces. The axis of the cylinder, coinciding with the axis of sample rotation, is taken to be the laboratory y axis [17] and the flat faces lie in the laboratory xz plane (see Fig. 1). Moreover, the experimental observations indicating breakdown of the smectic layering during realignment implies that the magnitude of the interaction of the mesogens with the applied external magnetic field is comparable to the interaction promoting the formation of the layers. This situation is similar to that of System I described in Ref. [17].

Since the experiments indicate that the layered structure is disrupted during the realignment process, it is not appropriate to use the macroscopic continuum methods often used to model liquid crystalline systems, and it is for this reason that we have chosen to use a microscopic simulation technique. This, in turn, restricts the size of the simulation box that can be used because such microscopic simulation techniques are computationally more intensive.

Sections V A–V C outline the simulation technique used and the changes required in order to confine the system to a cylindrical geometry. The small-angle x-ray scattering patterns were computed as described in Ref. [17] and the method is given in the Appendix.

A. Dissipative particle dynamics of nematic mesogens

The DPD methodology for the simulation of orientationally ordered phases has been described in detail previously [18–21] and will only be summarized here. The equations of motions governing the behavior of particles of identical mass are

$$d\boldsymbol{r}_i = \boldsymbol{v}_i dt \tag{3}$$

and

$$m \cdot d\boldsymbol{v}_i = (\boldsymbol{f}_C + \boldsymbol{f}_D + \boldsymbol{f}_R)dt, \tag{4}$$

where $\boldsymbol{r}_i$ and $\boldsymbol{v}_i$ are the position and velocity of the ith particle, respectively. The conservative force, $\boldsymbol{f}_C$ arises from a pair-wise potential, while $\boldsymbol{f}_D$ and $\boldsymbol{f}_R$ represent the effective dissipative and fluctuating forces, respectively. The potential giving rise to the conservative forces acting on identical particles has the form of a sticky soft interaction,

$$U_C(r_{ij}) = \begin{cases} \dfrac{a\varepsilon_{ij}^{\mathrm{rep}} r_c}{2}\left(1 - \dfrac{r_{ij}}{r_c}\right)^2 & r_{ij} < r_c \\ -\dfrac{a\varepsilon_{ij}^{\mathrm{att}} r_c}{2}\left(1 - \frac{r_{ij}}{r_c}\right)^2 & r_{ij} < r_c + \delta r \\ 0 & r_{ij} > r_c + \delta r, \end{cases} \tag{5}$$

where a is the force parameter, setting the overall repulsion strength between particles, $\varepsilon_{ij}^{\mathrm{rep}}$ and $\varepsilon_{ij}^{\mathrm{att}}$ modulate the repulsive and attractive interactions, respectively, r_c is the cutoff radius of the repulsive interaction, and r_{ij} the distance between the particles. The attractive interaction corresponding to a sticky potential operates in a thin shell of width δr around the particle. We have here set $\delta r = 0.1 r_c$. Our choice for the form of the attractive interaction has been made in the spirit of the DPD framework though other forms can be used [2]. The conservative force $\boldsymbol{f}_C$ acting on the ith particle is then simply given by

$$f_C(r_{ij}) = \begin{cases} a\sum\limits_j \varepsilon_{ij}^{\mathrm{rep}}\left(1 - \dfrac{r_{ij}}{r_c}\right) & r_{ij} < r_c \\ -a\sum\limits_j \varepsilon_{ij}^{\mathrm{rep}}\left(1 - \dfrac{r_{ij}}{r_c}\right) & r_{ij} < r_c + \delta r \\ 0 & r_{ij} > r_c + \delta r, \end{cases} \tag{6}$$

where $\hat{\boldsymbol{r}}_{ij}$ is the unit interparticle. The dissipative force $\boldsymbol{f}_D$ is defined as a quantity proportional to the relative velocity between the particles,

$$\boldsymbol{f}_D = \gamma \sum_j w_c^2(r_{ij}) \boldsymbol{v}_{ij}^{\parallel}. \tag{7}$$

Here $\boldsymbol{v}_{ij}^{\parallel}$ is the projection of the relative velocity on the vector $\hat{\boldsymbol{r}}_{ij}$ and $w_c(r_{ij}) = 1 - r_{ij}/r_c$ when $r_{ij} < r_c + \delta r$ and zero elsewhere. The dissipation strength is determined by γ, and the corresponding effective random force is defined as

$$\boldsymbol{f}_{\mathrm{R}} = \sigma\xi(t) w_{\mathrm{c}}(r_{ij}) \hat{\boldsymbol{r}}_{ij} / \sqrt{dt}, \tag{8}$$

where $\xi(t)$ is a white-noise random term. A fluctuation-dissipation relation holds for the parameters of the dissipative and random forces, $\sigma^2 = 2\gamma k_B T$.

In the simulations below we make use of reduced units where r_{c}, m, and a are the units of length, mass, and force, respectively. The other units are defined in Table I in Ref. [17]. Each mesogenic unit in the simulation is a chain of n particles linked by elastic forces given by the classical spring force

$$\boldsymbol{f}_i = -k^*(r_{ij} - r_{\mathrm{eq}}) \hat{\boldsymbol{r}}_{ij} = -\boldsymbol{f}_j, \tag{9}$$

with k^* the reduced spring constant, r_{ij} the distance between the two joined particles and r_{eq} the equilibrium particle-particle distance. In addition, an elastic force with an elastic constant k_{e}^* is introduced between the first and last particles,

$$\boldsymbol{f}_1 = -k_e^*[r_{\mathrm{ln}} - (n-1) r_{\mathrm{eq}}] \hat{\boldsymbol{r}}_{\mathrm{ln}} = -\boldsymbol{f}_n. \tag{10}$$

This force primarily determines the linear extent of the mesogenic unit and random coils are obtained when it is omitted.

A cylindrical simulation box is used, centered at the origin. The radius R of the box is larger than its thickness and the axis of the cylinder lies along the laboratory y axis, coinciding with the direction of sample rotation. The flat faces of the cylinder lie in the laboratory xz plane. The mesogenic units are radially confined by surrounding isotropic coils. These coils are in turn confined to the simulation box by the application of short-range external forces. A radial force is applied to each particle at the curved surface of the cylinder, i,

$$\boldsymbol{f}_{i,xz} = k_{\mathrm{in}}^* \exp[-2.5(R - r_i)] \hat{\boldsymbol{r}}_i, \tag{11}$$

where $r_i = \sqrt{x_i^2 + z_i^2}$ and $\hat{\boldsymbol{r}}_i$ is the equivalent unit position vector of the particle with respect to the origin of the simulation cylinder. Note that this force only acts in the laboratory xz plane. The cutoff distance of this force was taken to be 2.5 particle radii so that in the simulations described below it only acts on the random coils near the edge of the simulation sphere. In addition a confining force was applied to each particle at the two flat surfaces of the cylinder at $y=0$ and $y=D$,

$$\boldsymbol{f}_{i,y} = \begin{cases} k_{\mathrm{in}}^*(1 - e^{2.5 y_i}) \hat{y} & y_i \le 0 \\ -k_{\mathrm{in}}^*(1 - e^{2.5(D - y_i)}) \hat{y} & y_i \ge D, \end{cases} \tag{12}$$

where $\hat{y}$ is the unit vector in the direction of the laboratory y axis. This force acts on the particles of both the random coils and the stretched mesogenic units. The stability of the smectic nanodroplet is, however, determined exclusively by the intermesogen interactions and the interactions of the mesogens with the random coils.

The equations of motion are solved numerically using the standard Verlet algorithm [22] coupled with a thermostat rescaling the velocities. Periodic boundary conditions were not applied as we are here dealing with a single nanodroplet in the simulation sphere. A linked-cell algorithm [22] was implemented.

Time steps of $dt = 0.04$ were used and the integration scheme yielded temperature fluctuations of less than 0.25% in the equilibrated state. A thermostat was applied every five time steps during the simulation run.

B. Realignment of mesogens in an external field

We shall now consider the alignment of the model mesogens in the nanodroplet under the influence of an external field. The applied field acts on the two terminal particles of the mesogenic unit (i.e., the end-to-end vector of the mesogen). The interaction used here corresponds to application of an external magnetic field and takes the form of an interaction between a field and an induced dipole,

$$E_{\mathrm{ext}}^*(t^*) = -\varepsilon_{\mathrm{ext}}^* P_2[\boldsymbol{\nu}_i(t^*) \cdot \boldsymbol{H}_{\mathrm{ext}}], \tag{13}$$

where $\varepsilon_{\mathrm{ext}}^*$ is the strength of the interaction and $\boldsymbol{\nu}_i(t^*)$ is the unit end-to-end vector of the ith mesogen and $\boldsymbol{H}_{\mathrm{ext}}$ is the unit vector of the external field. In the work presented here, the external field lies in the xz plane of the simulation sphere and at times $t^* < 0$ lies along the vertical axis of the simulation sphere. The forces $-\boldsymbol{F}_{\mathrm{ext}}$ and $\boldsymbol{F}_{\mathrm{ext}}$ derived from the potential, see Appendix A, were applied to the terminal particles 1 and n, respectively, so that the torque acts to rotate the mesogens about their centers.

C. System parametrization

The internal conformation of a model mesogenic unit is characterized by four parameters: the number of particles n, the two elastic spring constants, k^* and k_{e}^*, and the equilibrium distance between joined particles, r_{eq}. We have used identical mesogenic units, each containing ten particles with $r_{\mathrm{eq}} = r_{\mathrm{c}}$, $k^* = 100$, and $k_e^* = 500$, at a reduced density $\rho^* = 0.8$. The current simulations make use of a nanodroplet of a smectic phase suspended in an isotropic environment. The isotropic environment consists of mesgenic units in a random coil configuration; for these mesogens $k_e^* = 0$. The radius of the nanodroplet was taken to be $0.7R$, with R the radius of the cylindrical simulation box of thickness $T = 10$. On taking $R = 211$, each nanodroplet contained 12 606 stretched mesogens arranged in 20 smectic layers. There are 25 529 random coils in the isotropic environment. The value of the external confining force was $k_m^* = 24$.

A stable nanodroplet in the nematic phase is obtained on taking the strengths of the interparticle interactions between mesogens of the same configuration to be $\varepsilon_{ij}^{*\mathrm{rep}} = 24$ and $\varepsilon_{ij}^{*\mathrm{att}} = 48$, while those between particles in the stretched and random coil configurations (in the nematic and isotropic phases respectively) were $\varepsilon_{ij}^{*\mathrm{rep}} = 60$ and $\varepsilon_{ij}^{*\mathrm{att}} = 0$. This choice of parameters produced sufficient surface tension between the nanodroplet and its isotropic environment to suppress the exchange of mesogens between the two phases. A smectic configuration in the droplet can be produced only on invoking additional interactions, which induce a localization of the mesogens and thus introduce translational order. We have chosen to achieve this by increasing the attractive interactions between the terminal particles, number 1 and 10 and denoted as b, relative to the attractive interactions between

the main-chain particles of the mesogenic units denoted by a: $\varepsilon_{bb}^{*\mathrm{att}}=60$ against $\varepsilon_{aa}^{*\mathrm{att}}=48$. As mentioned previously, this corresponds to System I considered in Ref. [17]. Moreover, we shall take the interactions promoting the smectic layering between the mesogens to be weaker than the magnetic interactions between the mesogens and the magnetic field, and to this end choose $\varepsilon_{\mathrm{ext}}^{*}=0.15$. The smectic configurations produced in these two ways were found to be stable in the reduced temperature range $0.5 \geq T^{*} > 0.25$. The nanodroplets underwent a smectic-nematic transition at the upper limit of this interval.

The simulations were carried out at a reduced temperature close to the smectic-nematic transition. The realignment process was monitored for a reduced time of at least $t^{*}=4000$, following the rotation of the applied field.

VI. SIMULATION RESULTS

Simulations were carried out over the same angular rotations as those used in the experiments, and following calculation of the diffraction patterns (see Appendix B), the analysis techniques described in Sec. III were used to produce Fig. 6. For ease of comparison with the experimental data, a diffraction angle of 90° corresponds to the situation when the director is aligned with the applied field. When a small angular rotation (25°) is used, continuous rotation of the smectic layers is observed, as shown in Fig. 6(a)(i), and this is not accompanied by any significant decrease in the total scattered intensity. Over large angular rotations around $\phi=90°$ there is almost complete breakdown of the smectic layering within the sample, leading to a marked decrease in the scattered intensity during realignment [see Fig. 6(b)(ii)]. When the rotation is over an intermediate angle, the realignment process consists of some loss of the layer structure as the layers rotate to their final position. It should be noted that when the angle of rotation is close to 90° the realignment is degenerate since it can proceed either clockwise or anticlockwise. While this does contribute to the breakdown of the smectic layers, very similar results are obtained when the rotation angle is as low as 75°; as the rotation angle approaches 90°, the reduction in total scattered intensity becomes more pronounced. It should also be noted that the realignment process is much longer in the cases where there is a more significant decrease in the smectic organization [see, for example Fig. 6(b)]. Throughout the simulations the linewidth of the Bragg peaks is approximately constant, implying that there is no transient formation of the nematic phase during realignment. In all of the simulations the realignment process is accompanied by a permanent increase in Q, corresponding to a decrease in the layer spacing after rotation and the reasons for this change are unknown.

Further details of the realignment process in which $\phi=92°$ are shown in Fig. 7. Initially both the layer structure and the director are well ordered. However, the system becomes somewhat disorganized, both in terms of the layered structure and the orientational association of the molecules during the realignment process (see $t^{*}=1000$). Small domains of organization can still be seen, however, with some layered domains rotating in-plane in each direction. The bulk ordered structure then slowly returns over time, as was indicated in Fig. 6(b)(ii). At lower rotation angles, there is a combination of layer breakup and layer rotation, with some portions of the sample remaining intact during realignment.

VII. DISCUSSION

Our experimental and simulated results show an intriguing combination of contrasts and similarities to those presented by previous authors. In particular, no continuous rotation of the smectic layers is observed in the confined samples (continuous rotation of the director in the nematic phase can easily be achieved using fields of the intensity used here). Earlier experiments have indicated continuous in-plane rotation of either the smectic layers or the director when the sample is rotated by a small angle [8–10,14,15], whereas no realignment was observed under these conditions in our experiments on confined samples. In these earlier experiments, however, larger magnetic-flux densities were used (4–8 T), but even when repeating our experiments at 3 T, no continuous in-plane rotation of the layers was observed. This implies that either the alignment process is highly dependent on the material used, or that the confinement of the samples in thin films increases the resistance to continuous in-plane rotation of the smectic layers. It is well known that the surfaces play an important role in the configuration of the layered structure in smectic liquid crystal samples. Indeed, the formation of the classic bookshelf to chevron transition observed when cooling from Sm-A to Sm-C, a transition that is typically associated with a decrease in layer thickness, is due to the fact that the layer packing density remains fixed at the surfaces; since the layer thickness must reduce but the packing density at the surface is unchanged, the layers buckle in the center of the device. We propose that the lack of continuous in-plane smectic layer rotation in our experiments is due to the same phenomenon pinning the layer orientation at the surfaces, and is therefore due to the confinement of the samples in thin films.

When the sample rotation is ~90°, the simulated and experimental results, shown in Figs. 6(b) and 4(b), respectively, are strikingly similar. In each case no continuous rotation of the smectic layers is observed, and the reorientation is via sudden catastrophic breakdown of the smectic layers [see also Fig. 7(a)]. Interestingly, these results are also very similar to those from an earlier experiment in which NMR spectroscopy was used to monitor the director orientation [14], but are very different from those previously found using time-resolved x-ray scattering. In the NMR study, the signal corresponding to the director in its original position was seen to reduce while that corresponding to the final position increased—at no point was any intermediate director orientation observed. At the same time the total intensity of the NMR spectrum (an indication of the degree of nematiclike order in the system) reduced during the realignment process and subsequently increased once the process had completed. This is in direct agreement with our simulations, in which the sample appears to become disorganized in the early stages of the realignment process, as can be seen in Fig. 7; the NMR results indicate a loss of the nematiclike order within the

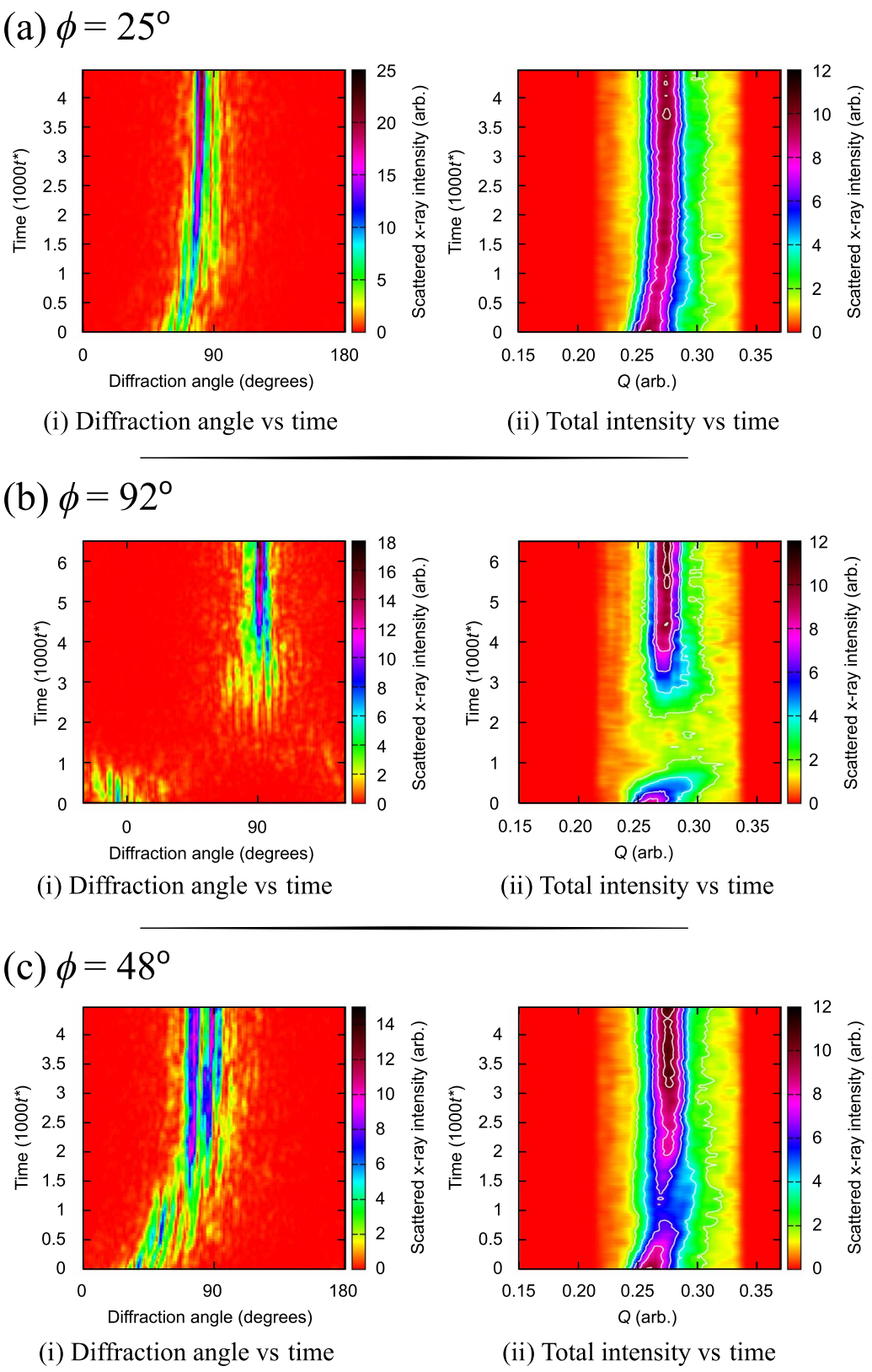

FIG. 6. (Color online) Simulated results with rotation angles of (a) ϕ=25°, (b) ϕ=92°, and (c) ϕ=48°. These are identical to the rotation angles investigated experimentally and shown in Fig. 4. (a) At small angular rotations there is continuous rotation of the smectic layers in order to bring the director into alignment with the applied field, and during realignment there is little or no change in the total scattered intensity. (b) At larger angular rotations the layer structure breaks down during the realignment process, leading to a significant reduction in the total scattered intensity. (c) When intermediate rotation angles a combination of layer breakdown and continuous rotation is observed.

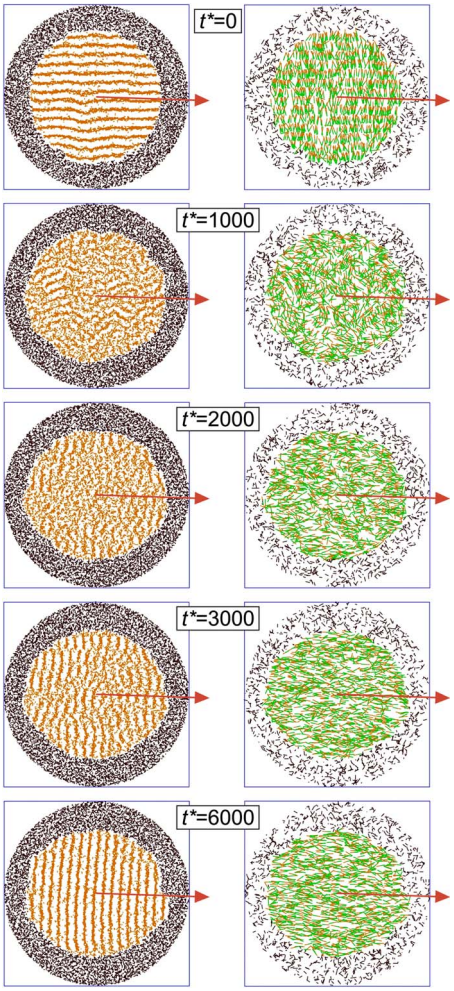

FIG. 7. (Color online) The nanosample structure during a simulation with a rotation angle of 92°. The arrow indicates the orientation of the applied magnetic field and the surrounding isotropic molecules have been made darker for ease of distinction. (a) The positions of the centers of mass of each molecule within the nanodroplet: the layered structure is lost during the initial part of the realignment process, but reforms slowly over time. (b) The orientation of the long axes of the molecules (only a random selection of molecules are shown for clarity): the sample appears to become significantly disorganized at $t^*=1000$. During the realignment process a multidomain structure can be seen in which some domains rotate clockwise and others anticlockwise (see $t^*=1000$).

layers while our x-ray scattering experiments show a breakdown in the smectic layer structure. The timescale of the realignment in the NMR experiment was, however, far longer (many minutes) than in our experiment, though this could be explained by increased viscous effects since the sample was held at 10 °C below the Sm-*A* to nematic transition temperature rather than 2 °C below as in our experiments. In addition, a significant mismatch between the initial and final intensities was also observed in Ref. [14], which the authors attributed to the presence of a broad distribution of layers in the final field-aligned state. This does not appear to be the case in our experiments possibly because our samples are confined to thin films. Our results are significantly different from those found previously using time-resolved x-ray scattering, where multiple realignment pathways were found with $\phi \sim 90°$ [10,11,15]. These experiments were carried out using very thick samples, however, and used significantly higher magnetic-flux densities (~8 T), though it is not clear why an increase in the applied field should produce such a different realignment process.

When an intermediate rotation angle of ~45° is used, our simulations indicate a realignment mechanism that involves both layer rotation and a decrease in the smectic organization, as shown in Fig. 6(c), while our experiments indicate only partial realignment through layer breakdown [Fig. 4(c)]. We have already observed that it is likely that the confining surfaces pin the smectic layers in place and thus introduce an energy barrier into the system that is not accounted for in our simulations. In our experiments it would appear that realignment can only take place through breakdown of the smectic layers because of this pinning phenomenon; while the simulations indicate a realignment mechanism that involves both layer rotation and layer breakdown, the experiments show partial realignment through layer breakdown alone.

While we cannot discount out-of-plane rotation of the smectic layers during the realignment process as a possible explanation for the decrease in the total scattered intensity observed experimentally, there are a number of reasons why this is unlikely. First, the striking similarity between the simulations and experiments presented here, combined with the absence of out-of-plane layer rotation in the simulations strongly indicates that it is layer breakdown that causes the decrease in the total scattered intensity. Second, since there is no direct interaction between the applied field and the layers themselves, any change in layer orientation must be either due to a change in the short-range molecular interactions present or a change in the director orientation, the latter requiring the presence of an out-of-plane torque. Since a mechanism by which the short-range molecular interactions could be altered in this case is unknown and the source of an out-of-plane torque in this experiment is unclear, it would appear sensible, in the absence of any evidence to the contrary, to assume that the layers do not rotate out-of-plane during realignment.

Similarly, while the formation of a transient Sm-*C* phase during realignment cannot be ruled out, there is no evidence to support its formation. No change in layer spacing is observed at any time during the experiments (there is a small decrease observed in the simulations during and after the reorientation). If the energy of the Sm-*A* and Sm-*C* were similar, one might expect to observe an induced Sm-*C* phase in the experiments where small rotation angles are used: it is clear from the experimental results that the layer orientation does not change in this situation, but the director could tilt within the layers, inducing a Sm-*C* phase and allowing the director to align with the applied field. This is clearly not the case, however, since the layer spacing change one would expect to accompany such a deformation is not observed, and there is no loss in the total scattered intensity that would be caused by buckling of the smectic layers into a chevron configuration.

VIII. CONCLUSIONS

As in previous studies, the realignment of Sm-*A* layers using a magnetic field has been shown to be a complex process that is highly dependent on the temperature of the sample. Here, we observe realignment only in the close vicinity of the Sm-*A* to nematic phase transition. This strong temperature dependence could be due to the sudden softening of the smectic layers close to the Sm-*A* to nematic transition [23], as well as pretransitional changes in the viscosity of the material. Our experiments on thin films of material have produced no evidence for intact rotation of the smectic layers even at small rotation angles, in contrast to previous experiments on bulk samples. At higher angles the signature signal of the layers in their original orientation decreases while that at the field-aligned position increases. This process is accompanied by a decrease in the total scattered intensity which is related to the integrity of the smectic layers. The smectic layers are, therefore, either moving away from the Bragg condition or are losing their integrity. This is in contrast to previous time-resolved x-ray scattering experiments where in-plane rotation of layers was observed over a wide range of rotation angles and temperatures [10,15]. When moderate realignment angles are used ($\sim 35-70°$) the layer reorganization usually only remains partially complete in our experiments.

A molecular-dynamics technique has been used to simulate the response of a thin cylindrical smectic nanosample to sudden reorientation within an applied magnetic field. While at small angular rotations continuous layer rotation is observed, when the rotation angle is increased the simulated and experimental results become very similar, with breakdown of the smectic layers observed followed by subsequent reformation in the field-aligned orientation. We propose that the lack of layer rotation observed in our experiments is due to pinning of the smectic layers by the glass substrates; realignment can only occur when there is a breakdown of the layered structure. The simulations show that there is a significant disruption of the liquid crystalline organization during realignment, indicating that it is this rather than out-of-plane rotation of the layers that is causing the decrease in the total scattered intensity in the experiments. The similarities between the experiment and the simulations imply that the energy associated with the formation of the smectic layers is indeed similar to the interaction energy inducing the realignment process.

With the addition of polyvinyl alcohol alignment layers the experimental realignment process is less consistent and the final field-aligned state typically consists of a range of layer orientations rather than the monodomain observed when no alignment layers are used. It is interesting to note that the surface treatment has a marked effect on the layer reorganization even in such thick samples (170 μm), though it is not yet clear whether the relative orientation of the rubbing direction and the aligning field has any influence.

ACKNOWLEDGMENTS

The authors would like to thank the Netherlands Organization for Scientific Research for making the facilities at the DUBBLE BM26B beam line available. The DUBBLE staff is thanked for their technical support during the experiments, especially Kristina Kvashnina and Giuseppe Portale. Thanks also to the EPSRC, U.K. for their financial support through Grant No. EP/D069793/1.

APPENDIX A: CALCULATION OF THE EXTERNAL FORCES ON THE MESOGEN

Here we shall consider the interaction, Eq. (13), between the unit end-to-end vector of a mesogen $\boldsymbol{\nu}=(\Delta x/r,\Delta y/r,\Delta z/r)$ and a magnetic field applied in the xz plane of the simulation box, $\boldsymbol{H}_{\text{ext}}=(H_x,0,H_z)$. Here $r=\sqrt{\Delta x^2+\Delta y^2+\Delta z^2}$ and $\Delta x=x_1-x_n$, $\Delta y=y_1-y_n$, and $\Delta z=z_1-z_n$. The subscripts 1 and n denote the two terminal particles of the mesogen. On substituting these values into Eq. (13) we find

$$E^*_{\text{ext}}(t^*)=-\varepsilon^*_{\text{ext}}P_2(\boldsymbol{\nu}_i\cdot\boldsymbol{H}_{\text{ext}})=-\frac{1}{2}\varepsilon^*_{\text{ext}}\left[\frac{\Delta x^2H_x^2}{r^2}+\frac{\Delta z^2H_z^2}{r^2}+\frac{2\Delta x\Delta zH_xH_z}{r^2}\right]-\frac{1}{2}. \tag{A1}$$

In order to calculate the force due to this potential, $\boldsymbol{F}=-\nabla E^*_{\text{ext}}$ we obtain the partial derivatives with respect to the Cartesian coordinates $\alpha=\Delta x,\Delta y,\Delta z$ using the property

$$\frac{\partial}{\partial\alpha}\left(\frac{1}{r^2}\right)=-\frac{2\alpha}{r^4}. \tag{A2}$$

In this way we find that the components of the forces are

$$F_x=-\frac{3\varepsilon^*_{\text{ext}}}{r}\left[\frac{\Delta xH_x^2}{r}\left(\frac{\Delta x^2}{r^2}-1\right)+\frac{\Delta x\Delta z^2H_z^2}{r^3}+\frac{\Delta zH_xH_z}{r}\left(\frac{2\Delta x^2}{r^2}-1\right)\right], \tag{A3}$$

$$F_y=-\frac{3\varepsilon^*_{\text{ext}}}{r}\left[\frac{\Delta x^2\Delta yH_x^2}{r^3}+\frac{\Delta y\Delta z^2H_z^2}{r^3}+\frac{2\Delta x\Delta y\Delta zH_xH_z}{r^3}\right], \tag{A4}$$

$$F_z=-\frac{3\varepsilon^*_{\text{ext}}}{r}\left[\frac{\Delta x^2\Delta zH_x^2}{r^3}+\frac{\Delta zH_z^2}{r}\left(\frac{\Delta z^2}{r^2}-1\right)+\frac{\Delta xH_xH_z}{r}\left(\frac{2\Delta z^2}{r^2}-1\right)\right]. \tag{A5}$$

The forces $\boldsymbol{F}$ and $-\boldsymbol{F}$ are now applied to particles 1 and n of the mesogen.

APPENDIX B: CALCULATION OF LOW-ANGLE X-RAY SCATTERING PATTERNS FROM SIMULATION RESULTS

The x-ray beam is incident on the cylindrical sample along its axis, which is also the axis of the rotation of the field, the fixed laboratory y axis. The planar detector is placed in the xz plane. For this geometry the scattering in-

tensity in the detector plane is calculated as [17]

$$I(q_x,q_z) = \sum_{j=1,N} e^{i(x_j q_x + z_j q_z)} \sum_{j'=1,N} e^{-i(x_j q_x + z_{j'} q_z)}, \qquad \text{(B1)}$$

where $i=\sqrt{-1}$ and the summations are carried out over the particles in the cylindrical smectic region. We have calculated the intensities on taking $q=\sqrt{q_x^2+q_z^2}=0.016$ so that only the first-order diffraction maxima appeared in the patterns. We note that a pair of maxima appear only when the Bragg condition, $q=\pm 2\pi/d$, is satisfied. Here d is the thickness of the smectic layer. The line joining the maxima lies perpendicular to the planes of the smectic layers. This procedure produces scattering patterns similar to those observed experimentally. We note here that virtually identical patterns are produced if only the terminal particles of each mesogen are included in the summation above.

[1] J. S. Patel and J. W. Goodby, J. Appl. Phys. **59**, 2355 (1986).
[2] J. S. Patel, S. D. Lee, and J. W. Goodby, Phys. Rev. A **40**, 2854 (1989).
[3] K. Nakayama, H. Moritake, M. Ozaki, and K. Yoshino, Jpn. J. Appl. Phys., Suppl. **34**, L1599 (1995).
[4] H. F. Gleeson and A. S. Morse, Liq. Cryst. **21**, 755 (1996).
[5] K. Nakayama, M. Ozaki, and K. Yoshino, Jpn. J. Appl. Phys., Suppl. **35**, 6200 (1996).
[6] I. Dierking, L. Komitov, and S. T. Lagerwall, Jpn. J. Appl. Phys., Suppl. **37**, L57 (1998).
[7] L. S. Matkin, H. F. Gleeson, L. J. Baylis, S. J. Watson, N. Bowring, A. Seed, M. Hird, and J. W. Goodby, Appl. Phys. Lett. **77**, 340 (2000).
[8] J. W. Emsley, J. E. Long, G. R. Luckhurst, and P. Pedrielli, Phys. Rev. E **60**, 1831 (1999).
[9] J. W. Emsley, G. R. Luckhurst, and P. Pedrielli, Chem. Phys. Lett. **320**, 255 (2000).
[10] W. Bras, J. W. Emsley, Y. K. Levine, G. R. Luckhurst, J. M. Seddon, and B. A. Timimi, J. Chem. Phys. **121**, 4397 (2004).
[11] A. S. Morse, H. F. Gleeson, and S. Cummings, Liq. Cryst. **23**, 717 (1997).
[12] A. Findon, H. F. Gleeson, and J. Lydon, Phys. Rev. E **62**, 5137 (2000).
[13] W. Bras, I. P. Dolbnya, D. Detollenaere, R. van Tol, M. Malfois, G. N. Greaves, A. J. Ryan, and E. Heeley, J. Appl. Crystallogr. **36**, 791 (2003).
[14] J. W. Emsley, J. E. Long, G. R. Luckhurst, and P. Pedrielli, Phys. Rev. E **60**, 1831 (1999).
[15] W. Bras, Y. K. Levine, and A. Polimeno Nucl. Instrum. Methods Phys. Res. B **238**, 1 (2005).
[16] H. Ogaki, K. Okumoto, A. Sugimura, and H. Zimmermann, Thin Solid Films **499**, 249 (2006).
[17] Y. K. Levine and W. Bras, Eur. Phys. J. E **25**, 5 (2008).
[18] Y. K. Levine and A. Polimeno, Eur. Phys. J. E **23**, 13 (2007).
[19] C. C. Liew and M. Mikami, Chem. Phys. Lett. **368**, 346 (2003).
[20] I. Vattulainen, M. Karttunen, G. Besold, and J. M. Polson, J. Chem. Phys. **116**, 3967 (2002).
[21] Y. K. Levine, A. E. Gomes, A. F. Martins, and A. Polimeno, J. Chem. Phys. **122**, 144902 (2005).
[22] D. Frenkel and B. Smit, *Understanding Molecular Simulation: From Algorithms to Applications* (Academic, San Diego, 1996).
[23] R. Bartonlino and G. Durand, Solid State Commun. **54**, 301 (1985).